





Two-site entanglement in the two-dimensional Hubbard model

Frederic Bippus ¹, Anna Kauch ¹, Gergő Roósz,² Christian Mayrhofer,¹ Fakher Assaad ^{3,4} and Karsten Held ¹

¹*Institute of Solid State Physics, TU Wien, 1040 Vienna, Austria*

²*HUN-REN Wigner Research Center for Physics, H-1525 Budapest, P.O.Box 49, Hungary*

³*Institut für Theoretische Physik und Astrophysik,
Universität Würzburg, 97074 Würzburg Germany*

⁴*Würzburg-Dresden Cluster of Excellence ct.qmat, Am Hubland, 97074 Würzburg, Germany*

(Dated: June 15, 2025)

The study of entanglement in strongly correlated electron systems typically requires knowledge of the reduced density matrix. Here, we apply the parquet dynamical vertex approximation to study the two-site reduced density matrix at varying distance, in the Hubbard model at weak coupling. This allows us to investigate the spatial structure of entanglement in dependence of interaction strength, electron filling, and temperature. We compare results from different entanglement measures, and benchmark against quantum Monte Carlo.

I. INTRODUCTION

Entanglement is one of the key manifestations of quantum mechanics and builds on correlations beyond the limits of what is classically possible¹. Despite its importance, quantifying and characterizing entanglement in strongly correlated electron systems remains a significant challenge, especially at finite temperatures. Here, the fundamental model is the Hubbard model which remarkably captures many essential features of strongly correlated electron systems, including superconductivity in cuprates^{2–4} and nickelates⁵, pseudogaps^{6–8}, kinks^{9,10}, waterfalls¹¹ and the Mott transition^{12,13}.

To this date, various approaches have been applied to study entanglement in the Hubbard model, yet little is known about the spatial structure of entanglement. On the one hand, multipartite entanglement probes such as the quantum Fisher information have proven to be valuable, because they offer experimental accessibility via susceptibility measurements^{14–18}. In particular, multipartite entanglement has been detected in the pseudogap¹⁹ and strange metal regime²⁰. However, the quantum Fisher information characterizes the entanglement depth of a system, offering no insight into the spatial structure of entanglement.

On the other hand, bi-partite entanglement in the pseudogap has been detected based on CDMFT²¹, a cluster extension to the dynamical mean field theory (DMFT). Both DMFT and CDMFT have also been applied to study entanglement at the Mott transition^{21–25}. CMDFT and similar calculations with exact diagonalization (ED)^{26,27} are however limited to small clusters and thus yield only little information on the spatial structure of entanglement.

Similarly limited to small two-dimensional systems, and by entanglement itself²⁸, are matrix product state (MPS) methods. Nevertheless, they have provided an in-depth analysis of momentum space entanglement in the ground state of the two-dimensional Hubbard model²⁹.

Besides these examples, entanglement has been studied quite intensively in the one-dimensional Hubbard

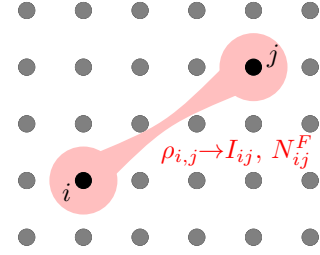


FIG. 1. Tracing out all but two lattice sites i, j provides the two-site reduced density matrix $\rho_{i,j}$, computed here from two- and four-point Green's functions with the p DΓA. From $\rho_{i,j}$, entanglement measures such as the mutual information I and fermionic negativity N^F between any two lattice sites can be evaluated. This entanglement includes spin and charge degrees of freedom.

model^{26,27,30–34}. Additionally, logarithmic corrections to the area law have been detected on the honeycomb lattice³⁵, and the entanglement spectra of exact excited eigenstates have been analyzed³⁶. On the practical side, the study of entanglement can be relevant, among others, to detect phase transitions^{27,37} and in quantum metrology³⁷.

In this paper, we aim at studying the spatial structure of entanglement in the two-dimensional Hubbard model at finite temperatures. To this end, we calculate the two- and four-point Green's functions with the parquet dynamical vertex approximation (p DΓA)^{38–40}. From these we obtain, with the methodology developed in Ref. 26, the two-site reduced density matrix (2s-RDM) $\rho_{i,j}$ for two lattice sites i, j at arbitrary distance, see Fig. 1. The 2s-RDM allows us in turn to calculate bi-partite entanglement measures such as the mutual information I_{ij} ^{41,42} and the (fermionic) negativity N_{ij}^F ^{43–46}.

Unlike the case of ED calculations in Ref. 26, we cannot benchmark the results against a direct evaluation of the 2s-RM, since we now consider significantly larger systems. To provide nevertheless an independent validation, we benchmark our results for one of the entanglement measures, the Rényi mutual information, against aux-

iliary field quantum Monte Carlo (QMC)^{47–52}. For the Hubbard model on a square lattice with weak to intermediate interaction strength U , we study how entanglement changes with U , filling n , and inverse temperature β . We find a close relation between entanglement and nesting of the Fermi surface. In contrast to entanglement in pure spin systems, our approach features entanglement between charge and spin degrees of freedom.

The outline of the paper is as follows: In Section II we introduce the von Neumann and Rényi mutual information as well as the fermionic negativity. In Section III the Hubbard model and the formalism to compute the 2s-RDM is recapitulated. We then apply this post-processing routine and benchmark it against QMC in Section IV. In Section V, the entanglement in the Hubbard model as function of distance is analyzed. We summarize our findings and discuss future research applications in Section VI.

II. ENTANGLEMENT MEASURES

Based on the 2s-RDM, any bi-partite density matrix based entanglement measure between two lattice sites i, j can be calculated. Since our calculations are at finite temperatures, we consider entanglement of mixed states. As there is not one definitive measure for entanglement, we will proceed by focusing on an "upper bound" and a "lower bound" for entanglement, such that both measures combined provide a complete picture.

As the first entanglement measure, we consider the mutual information^{41,42}. The mutual information is defined through the von Neumann entropy as a measure of all correlations in a system

$$I_{ij} \equiv \text{tr}[\rho_{ij} \ln \rho_{ij}] - 2 \text{tr}[\rho_i \ln \rho_i], \quad (1)$$

where $\rho_i = \text{tr}_j \rho_{ij} = \rho_j = \text{tr}_i \rho_{ij}$ is the one-site reduced density matrix. $I = 0$ corresponds to a separable and completely uncorrelated system, while $I > 0$ indicates entanglement but also classical correlations between i and j . We elaborate on this by showing analytical results for the antiferromagnetic Heisenberg dimer in Appendix A. Since the mutual information does not discriminate between quantum and classical correlations, it is an upper bound to entanglement, in the sense that zero mutual information implies no correlation and consequently no entanglement. A maximum is reached at $I = 2 \ln(\dim \rho_i) = 2 \ln(4)$, with 4 spin and charge degrees of freedom per site.

For comparison with QMC, the Rényi mutual information^{51,53} is computed as well

$$I_{ij}^R \equiv \ln[\text{tr} \rho_{ij}^2] - 2 \ln[\text{tr} \rho_i^2]. \quad (2)$$

The latter differs from the mutual information by the exponent by which ρ contributes, here 2, i.e., ρ^2 .⁵⁴ Due to its possible negativity^{55,56}, I^R is not a well-defined entanglement measure.

Besides the "upper bound" I_{ij} , we consider as a "lower bound" the negativity N . It investigates the physicality of the density matrix under the application of the partial transpose on site j only. Here, the partial transpose acts on any operator O in the Hilbertspace of $i \cup j$, and is elementwise defined as

$$\langle \psi_i, \psi_j | O^{T_j} | \bar{\psi}_i, \bar{\psi}_j \rangle \equiv \langle \psi_i, \bar{\psi}_j | O | \bar{\psi}_i, \psi_j \rangle. \quad (3)$$

If a density matrix is separable $\rho_{ij} = \rho_i \otimes \rho_j$, its partial transpose $\rho_{ij}^{T_j} = \rho_i \otimes \rho_j^T$ remains a physical density matrix and is positive semi-definite. Conversely, if the partial transpose $\rho_{ij}^{T_j}$ is not physical, the density matrix is not separable^{43,44}. To detect an unphysical partially transposed density matrix, one investigates if $\rho_{ij}^{T_j}$ is positive semi-definite, by summing over all its negative eigenvalues λ

$$N \equiv - \sum_{\lambda < 0} \lambda. \quad (4)$$

If the negativity N is non zero, the original matrix ρ_{ij} is not separable. The opposite statement is not true, since bound entangled states may exist with $N = 0$. Therefore, the negativity provides a lower bound to entanglement. Oftentimes, the negativity is rewritten in terms of the trace norm $\|\rho\|_{\text{tr}} = \sqrt{\text{tr}(\rho \rho^\dagger)}$ as⁵⁷

$$N = \frac{\|\rho_{ij}^{T_j}\|_{\text{tr}} - 1}{2}. \quad (5)$$

The measure is closely related to the logarithmic negativity $E_N = \log_2 \|\rho_{ij}^{T_j}\|_{\text{tr}}$ ^{57,58}. Unfortunately, the negativity cannot be directly applied to fermionic systems⁵⁹, as illustrated in Appendix B.

Instead of the negativity, we thus consider a recent extension thereof, based on the partial time-reversal transformation^{45,46}. We adapt the definition of the partial time-reversal operation from Shapourian *et al.*⁴⁶ to the case of a two-site density matrix with spin 1/2 particles. The partial time-reversal operation applied on an operator O yields

$$\langle \psi_i, \psi_j | O^{\text{TR}_j} | \bar{\psi}_i, \bar{\psi}_j \rangle \equiv \langle \psi_i, \bar{\psi}_j | O | \bar{\psi}_i, \psi_j \rangle (-1)^\phi \quad (6)$$

where the phase factor

$$\phi = \frac{n_i(n_i + 2)}{2} + \frac{\bar{n}_i(\bar{n}_i + 2)}{2} + \bar{n}_j n_j + n_i n_j + \bar{n}_i \bar{n}_j + (\bar{n}_i + \bar{n}_j)(n_i + n_j) \quad (7)$$

is given in terms of the number of electrons $n_i = n_{i,\uparrow} + n_{i,\downarrow}$ of each matrix element. For example $|\uparrow, \uparrow\rangle\langle\uparrow, \uparrow|$ has $n_i = \bar{n}_i = 1$ and $n_j = \bar{n}_j = 2$. In simple terms, this accounts for the number of minus signs picked up by permuting the fermionic operators in the process of taking the partial transpose. Equivalently to Eq. (5), the fermionic negativity is

$$N^F \equiv \frac{\|\rho_{ij}^{\text{TR}_j}\|_{\text{tr}} - 1}{2}. \quad (8)$$

And similar to the partial transpose, the eigenvalues of ρ_{ij}^{TR} are only negative if ρ_{ij} is not separable. Therefore, a non-zero fermionic negativity detects an entangled state. Moreover, one expects that any entangled state will necessarily lead to a nonzero fermionic negativity⁴⁵.

In Appendix B, we compare results from the four measures discussed here, i.e., I , I^R , N , and N^F , as well as the non-freeness^{60,61}.

III. MODEL AND METHOD

We investigate the one-band Hubbard model with nearest neighbor (NN) hopping t

$$H = - \sum_{\langle ij \rangle, \sigma} t \left(c_{i, \sigma}^\dagger c_{j, \sigma} + c_{j, \sigma}^\dagger c_{i, \sigma} \right) + U \sum_i n_{i, \uparrow} n_{i, \downarrow} - \mu \sum_{i, \sigma} n_{i, \sigma}, \quad (9)$$

where μ is the chemical potential, U the onsite Coulomb repulsion, $n_{i, \sigma} = c_{i, \sigma}^\dagger c_{i, \sigma}$ the occupation number operator, and $\hat{c}_{i, \sigma}^{(\dagger)}$ is the fermionic annihilation (creation) operator that annihilates (creates) an electron at site i with spin σ . We consider the square lattice in the paramagnetic phase, which implies $SU(2)$ symmetry. The Fourier transform of the kinetic term gives, for the NN hopping, the tight-binding dispersion relation

$$\varepsilon_{\mathbf{k}} = -2t(\cos k_x + \cos k_y), \quad (10)$$

where the momentum $\mathbf{k} = (k_x, k_y)$ is measured in units of the inverse of the lattice constant a . In the following, we set $\hbar = k_B = a = 1$ and measure all quantities in units of $t \equiv 1$.

To solve the Hubbard model, p DFA in the multi boson exchange formalism is applied⁶². For vertices and the self-energy, calculations are performed on a 16×16 momentum grid with periodic boundary conditions. A 10 times finer momentum grid is applied for sums over one-particle Green's function (coarse graining⁶³). For comparison with QMC, data without coarse graining is used. The difference in the entanglement measures between results with and without coarse graining is shown in Appendix C.

A. Parquet dynamical vertex approximation

The p DFA method uses as its basis the local two-particle fully irreducible vertex Λ , which is obtained from the solution of the DMFT impurity problem. In this work, the DMFT was solved with the continuous-time QMC in the hybridization expansion as implemented in the *w2dynamics* code⁶⁴. The resulting Λ is then used as input to the parquet equations.

The parquet equations are a set of exact relations between different classes of two-particle vertices and between the self-energy and the full two-particle vertex^{65,66}. A good introduction to the formalism is provided in⁶⁷. In this work, we use data generated with the multi-boson exchange implementation of the method as presented in^{62,68}. This allows for a careful treatment of the Matsubara frequency asymptotics needed in calculations of infinite sums. For some of the values of the parameters (i.e., for $U = 2$ and $U = 3$ out of half-filling), the parquet approximation (PA) was used. In the PA, the fully irreducible vertex Λ is approximated as U . While for weak coupling at $U = 2$, the p DFA is essentially reduced to PA for the range of the temperatures considered (Λ from DMFT is practically equal to U), for $U = 3$ this is not the case and we show results for both, p DFA and PA, in the half-filled case.

The p DFA is the computationally most involved diagrammatic extension of the DMFT⁴⁰ and therefore currently only relatively high temperatures and small grid sizes are available (there are, however, promising computational developments⁶⁹). The reason for this is that the vertices retain their full frequency and momentum dependence that reflects best spatial correlations. The method treats, by construction, all scattering channels equally, as well as the interplay between them. In cases where a clear dominance of one scattering channel is present, a simpler approach that retains dependence on one momentum only – the transfer momentum in the dominant channel – can be used. This simplification lies at the core of the ladder DFA method⁴⁰.

B. Calculating 2s-RDM from p DFA output

The 2s-RDM can be calculated as a postprocessing step using the method developed in Ref. 26, where the Heisenberg equation of motion links all symmetry-allowed matrix elements of ρ_{ij} to frequency sums over two- and four-point Green's functions. While all the details are provided in Ref. 26, we briefly sketch here which quantities obtained from p DFA are used in calculations in this work.

For completeness and also to introduce the notation, we start with the definition of the one-particle Green's function

$$G^k = - \sum_{i,j} \int_0^\beta d\tau e^{i\nu\tau} e^{-i\mathbf{k}(\mathbf{r}_i - \mathbf{r}_j)} \left\langle T_\tau \hat{c}_{i,\sigma}(\tau) \hat{c}_{j,\sigma}^\dagger(0) \right\rangle, \quad (11)$$

with τ denoting the imaginary time and $\beta \equiv 1/T$ the inverse temperature. We use a joint four-vector notation in which $k = (\nu, \mathbf{k})$ labels the combination of discrete fermionic Matsubara frequency $\nu_n = \frac{(2n+1)\pi}{\beta}$, $n \in \mathbb{Z}$, and momentum vector \mathbf{k} . We omit the spin index of G^k , since due to $SU(2)$ symmetry the one-particle Green's function is the same for both spins.

Analogously, we define the two-particle (four-point) Green's function

$$G_{\sigma_1 \dots \sigma_4}^{kk'q} = \sum_{i,j,l,m} e^{i\mathbf{k}\mathbf{r}_i} e^{-i(\mathbf{k}+\mathbf{q})\mathbf{r}_j} e^{i(\mathbf{k}'+\mathbf{q})\mathbf{r}_l} e^{-i\mathbf{k}'\mathbf{r}_m} \times \int_0^\beta d\tau_1 \int_0^\beta d\tau_2 \int_0^\beta d\tau_3 e^{i\nu\tau_1} e^{-i(\nu+\omega)\tau_2} e^{i(\nu'+\omega)\tau_3} \times \left\langle T_\tau \hat{c}_{i,\sigma_1}(\tau_1) \hat{c}_{j,\sigma_2}^\dagger(\tau_2) \hat{c}_{l,\sigma_3}(\tau_3) \hat{c}_{m,\sigma_4}^\dagger(0) \right\rangle, \quad (12)$$

where we additionally have a bosonic frequency-momentum index $q = (\omega, \mathbf{q})$, with bosonic Matsubara frequency $\omega_n = \frac{2\pi n}{\beta}$ and momentum \mathbf{q} . Due to SU(2) symmetry, the number of spin components that need to be computed reduces to the following: $G_{\sigma\sigma'\sigma'}$, which we will denote by $G_{\sigma\sigma'}$, and $G_{\sigma(-\sigma)(-\sigma)\sigma}$, which can be shown to be equal to $G_{\sigma\sigma} - G_{\sigma(-\sigma)}$. Furthermore, since $G_{\sigma\sigma'} = G_{(-\sigma)(-\sigma')}$, we only need to compute $G_{\uparrow\uparrow}$ and $G_{\uparrow\downarrow}$ ⁴⁰.

The full two-particle vertex F is defined by subtracting disconnected parts of the four-point Green's function and by "amputating the legs", which results in the following expression⁴⁰

$$G_{\sigma\sigma'}^{kk'q} = G^k G^{k'} \delta_{q0} - G^k G^{k+q} \delta_{kk'} \delta_{\sigma\sigma'} - G^k G^{k+q} F_{\sigma\sigma'}^{kk'q} G^{k'} G^{k'+q}. \quad (13)$$

To make the connection between the vertex and the physical susceptibilities, we introduce the following spin combinations: magnetic $X_m = X_{\uparrow\uparrow} - X_{\uparrow\downarrow}$ and density $X_d = X_{\uparrow\uparrow} + X_{\uparrow\downarrow}$ where X is any two-particle quantity such as G , F or the susceptibility χ . That is, in this notation, the physical susceptibility in the $\alpha = m, d$ channel is given by

$$\chi_\alpha^q = -2 \sum_k G^k G^{k+q} - 2 \sum_{k,k'} G^k G^{k+q} F_\alpha^{kk'q} G^{k'} G^{k'+q}. \quad (14)$$

Following Ref. 26, we can directly compute some contributions to the 2s-RDM from the susceptibilities. Other contributions require the screened interaction W_α^q defined as^{62,70}

$$W_\alpha^q = U_\alpha - \frac{1}{2} U_\alpha \chi_\alpha^q U_\alpha, \quad (15)$$

where $U_d = U$, $U_m = -U$. The susceptibility χ and F are connected to the fermion-boson irreducible vertex γ_α^{kq} through⁷⁰

$$\gamma_\alpha^{kq} = \frac{1 + \sum_{k'} F_\alpha^{kk'q} G^{k'} G^{k'+q}}{1 - \frac{1}{2} U_\alpha \chi_\alpha^q}. \quad (16)$$

Both W and γ are direct output of the p DFA in the multi-boson exchange implementation^{62,68}. In this implementation, we can also calculate F more memory-efficiently. Instead of the full F , we consider T , γ and W related to F through:

$$F_\alpha^{kk'q} = T_\alpha^{kk'q} + \gamma_\alpha^{kq} W_\alpha^q \gamma_\alpha^{k'q}. \quad (17)$$

The advantage is that the memory-intensive T can now be computed on a smaller frequency box than F , while $\gamma W \gamma$ use a larger frequency box. This way, we can provide better asymptotics than direct calculation of the memory-intensive F . This is particularly important for contributions to the 2s-RDM coming from derivatives of the four-point Green's function that result in the full vertex multiplied by frequencies – the additional two-point Green's functions that appear in those contributions guarantee that these terms do not diverge, but a careful asymptotic treatment as explained in the Appendix of Ref. 26 is required.

IV. COMPARISON TO QUANTUM MONTE CARLO

In this section, we benchmark the results for the mutual information based on Rényi entropy obtained from 2s-RDM with p DFA against direct Quantum Monte Carlo calculation. Since p DFA is not an exact method, there will be some deviations to QMC, especially at larger U and lower T . For $\beta = 5$ and $U = 2$, on the other hand, it has been shown that there is quantitative agreement between the parquet equations result (even in parquet approximation) and QMC^{72,73}, whereas for $U = 3$ differences start to be visible⁷². Here we use the same parameters and compare the Renyi mutual information for a 16×16 lattice with periodic boundary conditions.

A. Obtaining Renyi entropy from QMC

QMC methods solve the many-body problem by stochastically sampling the high-dimensional integral of the grand canonical ensemble. Where sign-problem-free formulations exist, this approach allows for error-controlled solutions, making it the method of choice for benchmarking other numerical methods. We use the algorithms for lattice fermions (ALF) package, which provides an implementation of the finite-temperature and projective auxiliary-field quantum Monte Carlo algorithm⁵⁰, which constructs the Rényi mutual information from two independent simulations of the system^{51,52}. For the calculations we have used a symmetric Trotter decomposition with an imaginary time step set to $\Delta\tau t = 0.1$. At $U/t = 4$ Fig. 2 of Ref. 50 shows that this produces a negligible systematic error for the energy.

B. Comparison between p DFA and QMC

To compare the two numerical methods, we compute the Rényi mutual information between two lattice sites separated by $\Delta \equiv \mathbf{r}_j - \mathbf{r}_i = (\Delta_x, \Delta_y)$. In the entire comparison, we do not apply coarse graining in p DFA as QMC simulates a finite 16×16 system.

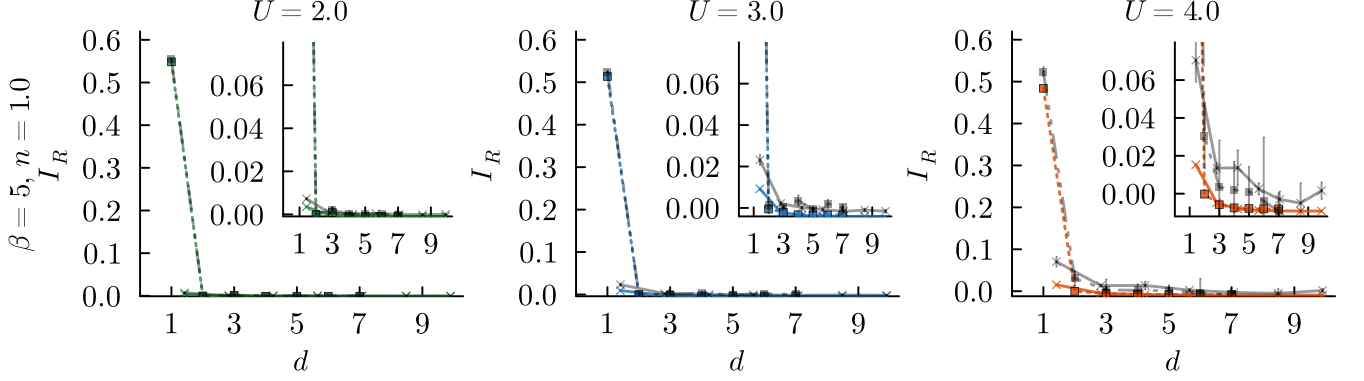


FIG. 2. Rényi mutual information I_R as a function of distance d comparing p DFA (color) and QMC (grey) for the 16×16 -site Hubbard model at half-filling and, from left to right, $U = 2, 3, 4$. Solid lines and crosses are measurements along the diagonal of the lattice $\Delta = (\Delta, \Delta)$, boxes and dotted lines are measured along the NN path $\Delta = (\Delta, 0)$. We denote the real distance $d = \sqrt{\Delta_x^2 + \Delta_y^2}$ from the reference site on the x -axis. Insets are the same plot with an enlarged y -axis. For $U = 2, 3$ the QMC error bars are smaller than the symbols. Errors only become significant in the inset for $U = 4$, here both the statistic and Trotter error are relevant.

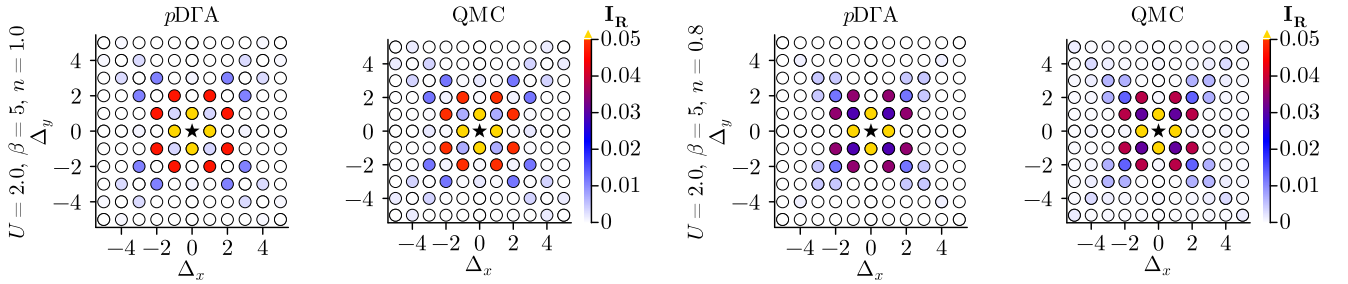


FIG. 3. Rényi mutual information I_R (false colors) between a reference point (star) and a second lattice site at distance (Δ_x, Δ_y) , comparing p DFA and QMC for $U = 2, \beta = 5$ and two fillings, i.e., $n = 1$ (half-filling, two leftmost panels) and $n = 0.8$ (two rightmost panels)⁷¹. Note that NN I_R is outside the color bar and marked in yellow; from left to right we have for NN: $I_{01}^R = 0.5484$, $I_{01}^R = 0.5540$; $I_{R,01}^R = 0.4982$, $I_{R,01}^R = 0.5031$.

Fig. 2 shows the Rényi mutual information I_R at half-filling ($n_i = n = 1$) and $\beta = 5$, for different values of U as a function of distance $d = \sqrt{\Delta_x^2 + \Delta_y^2}$. Dashed lines show I_R along the x -direction $\Delta = (\Delta, 0)$ and solid lines are data along the diagonal $\Delta = (\Delta, \Delta)$.

While the Rényi mutual information is large between NN neighbors, it drops off extremely rapidly already for the next-next nearest neighbor, necessitating the enlargement of the insets. This suggests only a weak entanglement, except for neighboring sites. Interestingly, we encounter a rarely observed negative Rényi mutual information at large distances.

As for the comparison between p DFA and QMC, the agreement for the smallest interaction $U = 2$ is very good, validating the developed p DFA calculation of the Rényi mutual information. For $U = 4$ and to a lesser extent $U = 3$, we find some quantitative though not qualitative discrepancy. The reasons for the observed differences are: (i) The computation of the 2s-RDM from p DFA requires infinite Matsubara sums and thus the knowledge of the two-particle vertex in a sufficiently large frequency range.

For higher values of U this range increases and the finite-box error grows. This deficiency can hopefully be cured with the application of novel vertex compression methods⁶⁹. (ii) With larger U there will be corrections to the the p DFA approximation of a local fully irreducible vertex. This is actually more severe for a small 16×16 cluster, than for an infinite lattice, since the momentum dependence of the fully irreducible vertex is more pronounced in small systems⁷⁴.

(iii) For $U = 4, \beta = 5$ the antiferromagnetic susceptibility is already very strongly enhanced to $\chi(\omega_n = 0, \mathbf{q} = (\pi, \pi)) \approx 30$ in QMC. In DMFT, antiferromagnetic order would have already set in (not shown). In the temperature regime where the susceptibility strongly increases, only a minor deviation of the onset temperature for this increase will result in largely different susceptibilities. Such a difference is observed for the susceptibility in Appendix D for $U = 4$; and Fig. 2 shows how this reflects in the Rényi mutual information.

In Fig. 3, we also present a real space map of the results for $U = 2$ at two different fillings $n = 1.0$ and 0.8 . The agreement between p DFA and QMC is again

very good, but for further neighbors the p DFA mutual information is slightly smaller, particularly upon doping. Note that the filling $n = 0.8$ is also observed at slightly different values of the chemical potential $\mu_{\text{QMC}} = 0.2610$, $\mu_{\text{DFA}} = 0.2667$. Interestingly, at half-filling there is an alternating pattern of sites with more and less Rényi mutual information, and thus supposedly entanglement. All of these alternations are however small compared to the NN I^R which has by far (even on another scale) the largest mutual information. This also holds for the conventional (non-Rényi) mutual information and other entanglement measures, and will be discussed in more detail in the next Section.

V. RESULTS

Having tested and demonstrated the reliability of 2s-RDM results obtained from p DFA in the previous section, we now turn to an analysis of the bi-partite entanglement structure of the 2D Hubbard model. We restrict ourselves to nearest-neighbor (NN) hopping on the square lattice in the weakly correlated Fermi liquid phase.

In Fig. 4, we investigate the structure of entanglement within real space for different values of interaction strength U , filling n , and inverse temperatures β . To obtain meaningful results, we combine the von Neumann mutual information (I , instead of the Rényi mutual information of the previous section; top) as an upper bound to entanglement, and the quantitatively unrelated fermionic negativity (N^F ; bottom) as a lower bound. Both measures follow the same qualitative behavior, proving that the observed structure indeed resembles the spatial structure of entanglement.

Entanglement is strong only for NN sites and rapidly decreases by approximately one order of magnitude for larger distances. However, this decrease is neither isotropic nor smooth as one might naïvely expect or has in a free electron gas scenario. In fact, entanglement is modulated by two main effects.

First, as a universal feature of our results, we observe that entanglement along the NN direction $\Delta = (\Delta, 0)$ is less long-ranged than entanglement close to the diagonal direction $\Delta = (\Delta, \Delta)$. This is a direct consequence of the NN hopping t and the connectivity between different sites. The connectivity of two sites is given by the number of paths that connect them with a specific number of NN hoppings. Comparing two sites that are separated from a reference site by the same number of NN hoppings (i.e., same "Manhattan distance"), we find that the connectivity grows the more diagonal a path becomes. This is illustrated for two example sites in Fig. 5. Hence, sites that are connected by diagonal paths are expected to be more strongly entangled.

Furthermore, we observe a second attenuating effect. Even in the weak-coupling Fermi liquid phase ($U = 2, 3, 4$), far from the antiferromagnetic phase and Mott transition, entanglement at half-filling exhibits a

checkerboard pattern, reflecting the inherent antiferromagnetic tendency of the square lattice NN-hopping Hubbard model and resembling Néel order itself. Entanglement favors sites whose spins have an antiferromagnetic alignment (compare the real space spin susceptibility in Fig. 10 with Fig. 4). The same pattern of entanglement remains in the noninteracting case $U = 0$ (Appendix E). That is, the Néel-like pattern does not necessitate strong interactions, but can also be caused by the perfect nesting of the Fermi surface²⁹ $\varepsilon_{\mathbf{k}+(\pi,\pi)} = -\varepsilon_{\mathbf{k}}$, which leads to a divergent spin susceptibility at $\mathbf{q} = (\pi, \pi)$ ⁷⁵.

Moreover, when a doping lifts this nesting effect and antiferromagnetism is suppressed, we observe at both $U = 0$ (Fig. 11) and finite U (Fig. 4 d/h)), that the checkerboard pattern vanishes. Note that at low filling $n \simeq 0.8$ our method encounters nonphysical density matrices due to finite numerical precision. Where such nonphysical negative eigenvalues were encountered, we optimize for the closest positive semi-definite density matrix with unity trace following Ref. 76. Conversely, larger interactions U act favorably towards the antiferromagnetism, and the checkerboard pattern becomes more pronounced (compare Fig. 4 a/e) vs. b/f)). In accordance with the growing correlation length at lower temperatures, we also observe that the alternating entanglement pattern becomes more pronounced and entanglement more long-ranged at $\beta = 14$ (compare Fig. 4 b/f) vs. c/g)).

In Fig. 6, we turn from the qualitative patterning to the quantitative changes of entanglement. Going away from half-filling which suppressed the alternating entanglement pattern in Fig. 4, we observe in Fig. 4 that the magnitude of entanglement actually increases in all three entanglement witnesses studied. This is a bit counter-intuitive, at least for the mutual information, since spin correlations are strongest at half-filling. However, the 2s-RDM also includes the charge degree of freedom, which opens an additional channel for entanglement away from half-filling.

VI. SUMMARY

In this paper, we provide proof of principle that the two-site reduced density matrix can in practice be computed from Green's function based methods. The comparison with QMC results for the Rényi mutual information validates our approach. This enables us to simulate systems beyond the limitations of other methods and to unveil the spatial structure of entanglement in the 2D Hubbard model.

As regards physics, we observe a strong entanglement between NN sites in the Hubbard model and further a checkerboard-like pattern of much smaller entanglement beyond NN sites. Entanglement is largest in the vicinity of the diagonal and suppressed along the horizontal/vertical directions. This diagonal pattern of entan-

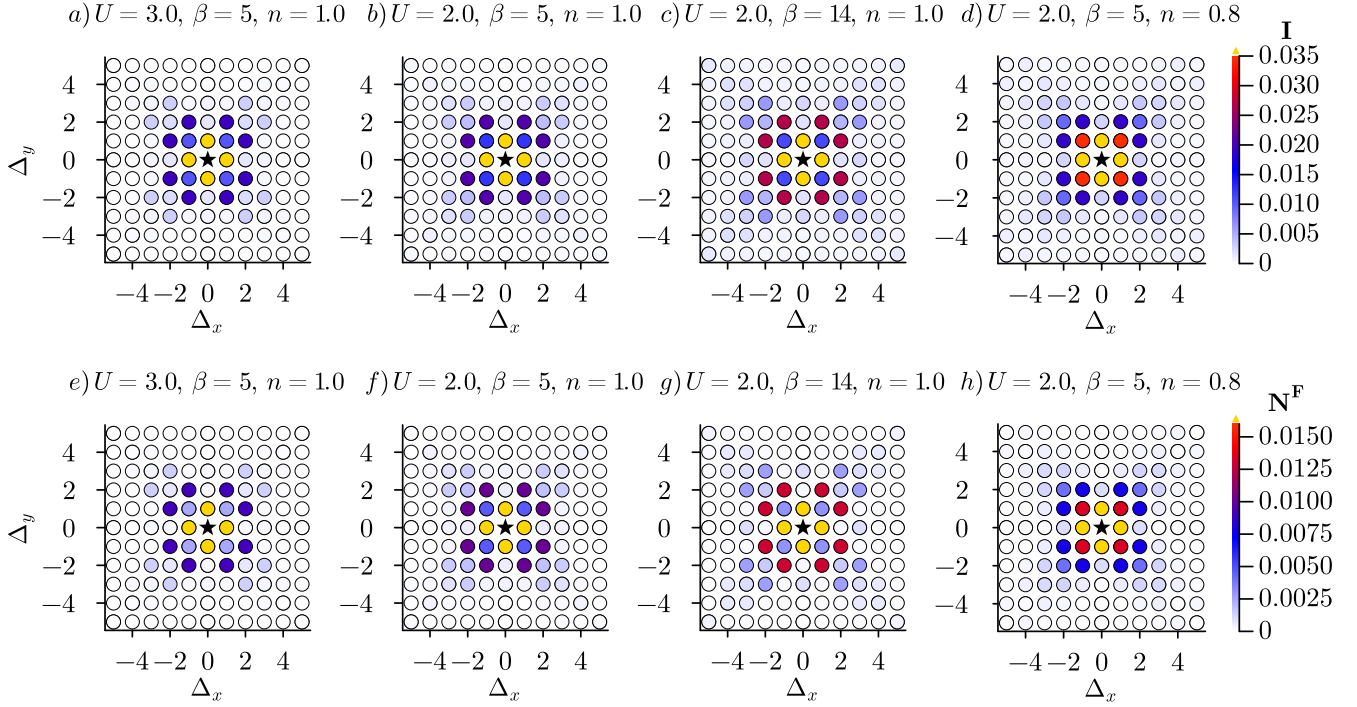


FIG. 4. a)-d) Mutual information I and e)-h) fermionic negativity N^F plotted as real space entanglement between lattice sites separated by $\Delta = (\Delta_x, \Delta_y)$ from a reference site marked by \star . From left to right we display (a,e) $U = 3, \beta = 5, n = 1$ where the yellow NN values are $I_{01} = 0.3014, N_{01}^F = 0.1646$; (b,f) $U = 2, \beta = 5, n = 1$ with $I_{01} = 0.3114, N_{01}^F = 0.1663$; (c,g) $U = 2, \beta = 14, n = 1.0$ with $I_{01} = 0.3196, N_{01}^F = 0.1732$; (d,h) and $U = 2, \beta = 5, n = 0.8$ with $I_{01} = 0.3181, N_{01}^F = 0.1417$.

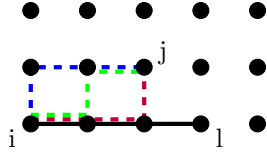


FIG. 5. Three different paths (dashed colored lines) connect sites i and j with three hoppings each, whereas there is just one path that connects i and l (solid line) with three hoppings. The Manhattan distance between i and j is the same as that between i and l , the Euclidean distance is even larger for the former pair.

glement can be explained by the larger number of possible hopping paths (to the same order in t) along the diagonal. And the checkerboard pattern is caused by the antiferromagnetic correlations which appear already at $U = 0$ for half-filling due to the perfect nesting of the Fermi surface. Upon increasing U , decreasing T and towards half-filling, the checkerboard entanglement pattern becomes more pronounced as do antiferromagnetic correlations. With the observed strong entanglement between antiferromagnetic NN pairs and the checkerboard (albeit weaker) entanglement pattern between more distant lattice sites, our work shows that the antiferromagnetic tendency of the Hubbard model is indeed a quantum (entanglement) effect.

Our observations of entanglement in the Hubbard

model demonstrate that our method can provide valuable insights into the quantum nature and entanglement of strongly correlated electronic systems. At present p DMFT is restricted to smaller values of U and lattices of the order of 16×16 . However, there are promising developments to overcome these limitations^{69,77}. The presented methodology can also be applied to obtain 2s-RDM from other approximate methods that provide one- and two-particle quantities, in particular ladder extensions of DMFT⁴⁰.

ACKNOWLEDGMENTS

FB, FA, and KH have been supported by the SFB Q-M&S (FWF project DOI 10.55776/F86); AK by project V 1018 of the Austrian Science Fund (FWF Grant DOI 10.55776/V1018); and GR by the QuantERA II project HQCC-101017733., National Research, Development and Innovation Office of Hungary NKFIH under Grant No. K128989, No. K146736, and by the Hungarian Loránt Eötvös mobility scholarship. Calculations have been done in part on the Vienna Scientific Cluster (VSC). For the purpose of open access, the authors have applied a CC BY-NC SA public copyright license to any Author Accepted Manuscript version arising from this submission.

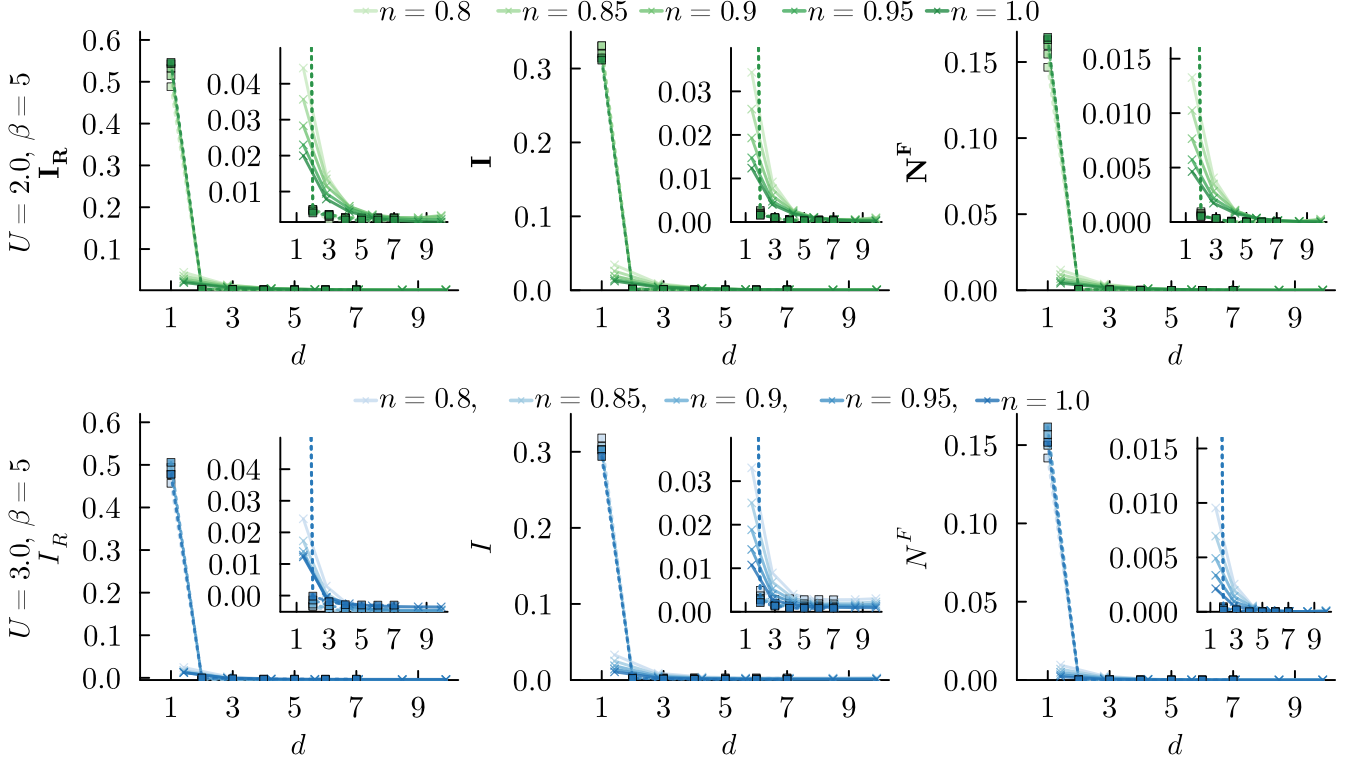


FIG. 6. Comparison of the Rényi mutual information I_R (left), mutual information I (middle), and fermionic negativity N^F (right) at distance d for different fillings n ; $U = 2$ (top) and $U = 3$ (bottom) at $\beta = 5$. From left to right we show Rényi mutual information I_R , mutual information I , and fermionic negativity N^F . Solid lines and crosses are measurements along the diagonal of the lattice while boxes and dotted lines are measured along the x (or y) direction. Insets are the same plot with an enlarged y -axis.

Appendix A: Entanglement in the Heisenberg dimer

While the mutual information is a faithful entanglement measure for pure states, it can not differentiate between classical correlations and quantum entanglement for mixed states⁴⁵. To illustrate this, we consider the strong coupling limit of the Hubbard model, the isotropic antiferromagnetic Heisenberg model⁷⁸

$$H = \sum_{\langle i,j \rangle} J \mathbf{S}_i \mathbf{S}_j, \quad (\text{A1})$$

and investigate the dimer as a particularly simple example. The density matrix in the basis $\{|\uparrow, \uparrow\rangle, |\uparrow, \downarrow\rangle, |\downarrow, \uparrow\rangle, |\downarrow, \downarrow\rangle\}$ is

$$\rho_{AB} = \frac{1}{4} \begin{pmatrix} 1+t_3 & & & t_1-t_2 \\ & 1-t_3 & t_1+t_2 & \\ & t_1+t_2 & 1-t_3 & \\ t_1-t_2 & & & 1+t_3 \end{pmatrix}, \quad (\text{A2})$$

with $t_1 = t_2 = t_3 = \frac{1-\alpha^{-4}}{3+\alpha^{-4}}$ and $\alpha = e^{-\beta J/4}$. As long as the condition $\sum_{i=1}^3 |t_i| \leq 1$ is fulfilled, it can be separated

into the form⁷⁹

$$\begin{aligned} \rho_{AB} = & \frac{1}{4} \sum_{i=1}^3 2|t_i| \left[\left\{ \frac{(\mathbb{I} - \sigma_i)_A}{2} \otimes \frac{(\mathbb{I} - \text{sign}(t_i) \sigma_i)_B}{2} \right\} \right. \\ & + \left. \left\{ \frac{(\mathbb{I} + \sigma_i)_A}{2} \otimes \frac{(\mathbb{I} + \text{sign}(t_i) \sigma_i)_B}{2} \right\} \right] \\ & + [(\mathbb{I})_A \otimes (\mathbb{I})_B] \left(1 - \sum_{i=1}^3 |t_i| \right). \end{aligned} \quad (\text{A3})$$

Here σ_i are the Pauli matrices. The separability condition is fulfilled for either $T = 0$ or $\beta J \leq \ln 3$. However, the mutual information

$$I = 2 \ln(2) + \frac{3-3\alpha^{-4}}{3+\alpha^{-4}} \ln(\alpha) - \ln(3\alpha + \alpha^{-3}) \quad (\text{A4})$$

at $\beta J = \ln 3$ is $I = \ln\left(\frac{2}{\sqrt{3}}\right) > 0$. Hence, while we know that the system is separable at $\beta J = \ln 3$, we find a non-zero mutual information measuring classical correlations and not entanglement. Likewise, the negativity can be computed. As we now consider a spin system, the partial transpose based negativity is applied, i.e., Eq. (4). This

yields

$$N = \begin{cases} \left| \frac{-1+3\alpha^4}{2(1+3\alpha^4)} \right| & \text{if } \beta J \leq \ln 3 \text{ or } T = 0 \\ 0 & \text{else} \end{cases}, \quad (\text{A5})$$

which indeed shows the correct limit of separability as it is an exact measure for qubits⁴⁴. However, the negativity may not detect non-separable states in larger systems. To conclude, the limitation of the negativity on mutual information require a mix of both or ideally even more entanglement measures to accurately detect entangled states.

Appendix B: Comparison of entanglement and correlation measures

The 2s-RDM formalism allows for the computation of a wide variety of entanglement measures. In the main text, we have limited ourselves to showing results for the von Neumann and Rényi mutual information and fermionic negativity (sec. II). Here, we want to compare these results to the plain vanilla negativity F from Eq. (4) (without fermionic phase ϕ) and the non-freeness^{60,61}.

First, the negativity defined through the partial transpose Eq. (4) does not indicate any entanglement at all beyond the NN pair, see Fig. 7; it is zero. This inability to faithfully detect entanglement in fermionic systems is to be expected^{45,46}. Second, the non-freeness of a density matrix ρ is defined by the relative entropy from the closest free state Δ

$$S(\rho||\Delta) = S(\rho) - S(\Delta), \quad (\text{B1})$$

where $\mathfrak{C} = S(\rho) = -\sum_{i=1}^{\dim \rho} \lambda_i \ln \lambda_i$ is the von Neumann entropy of a density matrix with eigenvalues λ . We can define two types of non-freeness. First, the non-freeness of the two site reduced density matrix \mathfrak{C}_2 with the closest free state given through the one that has the same one particle correlation functions as the original density matrix

$$\Delta_2 = \begin{pmatrix} c_{i\uparrow}^\dagger c_{i\uparrow} & c_{i\uparrow}^\dagger c_{j\uparrow} & & \\ c_{i\uparrow}^\dagger c_{j\uparrow} & c_{j\uparrow}^\dagger c_{j\uparrow} & & \\ & & c_{i\downarrow}^\dagger c_{i\downarrow} & c_{i\downarrow}^\dagger c_{j\downarrow} \\ & & c_{i\downarrow}^\dagger c_{j\downarrow} & c_{j\downarrow}^\dagger c_{j\downarrow} \end{pmatrix}. \quad (\text{B2})$$

Second, we can consider the distance-independent non-freeness of the one site reduced density matrix \mathfrak{C}_1 with free state

$$\Delta_1 = \begin{pmatrix} c_{i\uparrow}^\dagger c_{i\uparrow} & 0 \\ 0 & c_{i\downarrow}^\dagger c_{i\downarrow} \end{pmatrix}. \quad (\text{B3})$$

Both matrices are directly computable from the quantities defined in Ref. 26. In Fig. 7, we show the difference \mathfrak{C}_2 . For large d the result converges towards $2\mathfrak{C}_1$ (horizontal lines), showing that no correlations remain between distant sites.

To complete the comparison, the fermionic negativity and von Neumann mutual information both provide the same qualitative result and provide a clear picture of the genuine entanglement in the system. Meanwhile, the Rényi mutual information is not well suited as it becomes negative at large distances.

Appendix C: The impact of coarse graining

Fig. 8 shows a direct comparison of different interaction strengths U with and without coarse graining at $n = 1$ and $\beta = 5$. The coarse grained data has a smoother behavior than the data without. This is to be expected as the data better simulates an infinitely sized system where finite-size effects are not relevant.

Appendix D: Comparison of susceptibilities

In the calculation of the 2s-RDM the spin, density, and singlet susceptibilities of Eq. (14) contribute²⁶. Since these can be directly compared between p DFA and QMC they provide an excellent benchmark. We note that the definition of Eq. (14) corresponds to the following imaginary time correlators

$$\chi_m^q = \sum_j e^{-i\mathbf{q}(\mathbf{r}_i - \mathbf{r}_j)} \langle S_i^z(\tau) S_j^z \rangle, \quad (\text{D1})$$

$$\chi_d^q = \sum_j e^{-i\mathbf{q}(\mathbf{r}_i - \mathbf{r}_j)} \langle n_i(\tau) n_j \rangle - \beta \delta_q \langle n_i \rangle^2, \quad (\text{D2})$$

$$\chi_s^q = \sum_j e^{-i\mathbf{q}(\mathbf{r}_i - \mathbf{r}_j)} \langle c_{i\downarrow}(\tau) c_{i\uparrow}(\tau) c_{j\uparrow}^\dagger c_{j\downarrow}^\dagger \rangle. \quad (\text{D3})$$

We benchmark them as a function of \mathbf{k} along the high symmetry path $\Gamma - X - M - \Gamma$ through the Brillouin zone at imaginary time $\tau = 0$ in Fig. 9. Excellent agreement is observed at $U = 2$, which for the same parameters was also shown in Refs. 72 and 73 (where also parquet approximation, valid for $U = 2$ was applied). At $U = 4$ the agreement is only qualitative. The susceptibility at the M point is largely enhanced in QMC, a trend not yet observed in p DFA at this T and U as explained in the main text.

In the context of susceptibilities, we also show the $\chi^m(\tau = 0, \mathbf{r})$ susceptibility for $n = 1.0$ and $n = 0.8$ at $U = 2$, $\beta = 5$ in Fig. 10. This shows the antiferromagnetic Neel-like structure at half-filling which is suppressed off half-filling.

Appendix E: Mutual information in the non-interacting case

In this section, we discuss the two-point mutual information in the two-dimensional non-interacting lattice, at zero and finite temperatures. In this case, both the density matrix of the whole system and the reduced density

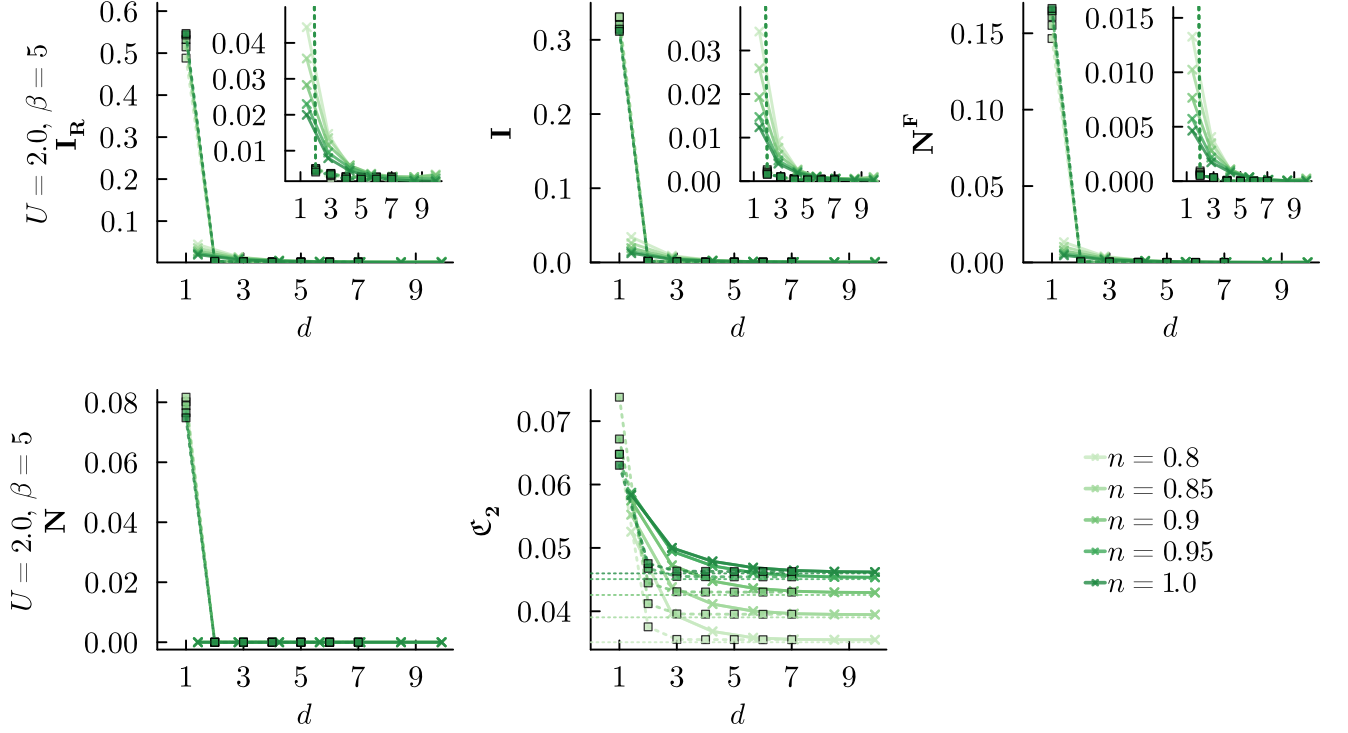


FIG. 7. Comparison of I_R , I , N^F , N and \mathfrak{C}_2 for $U = 2$ at $\beta = 5$ for a range of fillings n . We show Rényi mutual information I_R over distance d for $U = 2, 3, 4$ from left to right. Again solid lines and crosses are measurements along the diagonal of the lattice $\Delta = (\Delta, \Delta)$ while boxes and dotted lines are measured along the NN path $\Delta = (\Delta, 0)$ and we denote the real distance $d = \sqrt{\Delta_x^2 + \Delta_y^2}$ from the reference site on the x -axis. Insets are the same plot with an enlarged y -axis. The first row of data has already been displayed in fig. 6. For \mathfrak{C}_2 we observe that it converges towards two times the one-site limit $2\mathfrak{C}_1$ (thin constant line).

matrices are fermionic Gaussian matrices and standard techniques can be used⁸⁰. One only needs the occupation $\langle c_{i,\sigma}^\dagger c_{i,\sigma} \rangle$ and the hopping expectation value $\langle c_{i,\sigma}^\dagger c_{j,\sigma} \rangle$ to reconstruct the two site density matrix, and these values can be obtained as

$$\langle c_{i,\sigma}^\dagger c_{j,\sigma} \rangle = \frac{1}{L^2} \sum_k n_k e^{ik_x d_x + ik_y d_y} \quad (\text{E1})$$

where $n_k = 1/(\exp(\beta(\epsilon_k - \mu)) + 1)$ is the fermion occupation number, and (d_x, d_y) is the vector connecting sites i and j . In the special case of zero temperature, half-filling, and in the infinite size limit, one can perform the sum in E.q. (E1)

$$\langle c_i^\dagger c_j \rangle = \begin{cases} 0, & \text{if } (i_x - j_x)^2 - (i_y - j_y)^2 = 0 \\ -\frac{(-1)^{i_x - j_x} - (-1)^{i_y - j_y}}{\pi^2 [(i_x - j_x)^2 - (i_y - j_y)^2]}, & \text{otherwise} \end{cases} \quad (\text{E2})$$

In the general case, one computes Eq. (E1) numerically and gets the mutual information as

$$I = S_i + S_j - S_{i \cup j} \quad (\text{E3})$$

$$= 4 \ln \langle c_{i,\uparrow}^\dagger c_{i,\uparrow} \rangle \quad (\text{E4})$$

$$-4(\langle c_{i,\uparrow}^\dagger c_{i,\uparrow} \rangle - \langle c_{i,\uparrow}^\dagger c_{j,\uparrow} \rangle) \ln(\langle c_{i,\uparrow}^\dagger c_{i,\uparrow} \rangle - \langle c_{i,\uparrow}^\dagger c_{j,\uparrow} \rangle) \quad (\text{E5})$$

$$-4(\langle c_{i,\uparrow}^\dagger c_{i,\uparrow} \rangle + \langle c_{i,\uparrow}^\dagger c_{j,\uparrow} \rangle) \ln(\langle c_{i,\uparrow}^\dagger c_{i,\uparrow} \rangle + \langle c_{i,\uparrow}^\dagger c_{j,\uparrow} \rangle) \quad (\text{E6})$$

In the ground state of the half-filled infinite non-interacting system for large distances, this yields

$$I \approx \begin{cases} 0, & \text{if } (i_x - j_x)^2 - (i_y - j_y)^2 = 0 \\ 8 \left\{ \frac{(-1)^{i_x - j_x} - (-1)^{i_y - j_y}}{\pi^2 [(i_x - j_x)^2 - (i_y - j_y)^2]} \right\}^2, & \text{otherwise} \end{cases} \quad (\text{E7})$$

Here we expanded the $x \ln x + (1-x) \ln(1-x)$ function appearing in Eq. (E6) in a Taylor series up to second order around its maximum at $x = 1/2$, and in this way obtain a formula which is asymptotically exact for large distances. Numerical comparison shows that the formula has less than 5% error even when used for the nearest neighbors. Eq. (E7) means, that the two point mutual information decreases with the fourth power of the distance ($I \sim 1/d^4$) at zero temperature, and there is a checkerboard structure in I . This structure survives at finite temperatures, as it is shown in Fig. 11. If the system is not half-filled, there are no exactly vanishing correlations, and no checkerboard structure, as it is shown

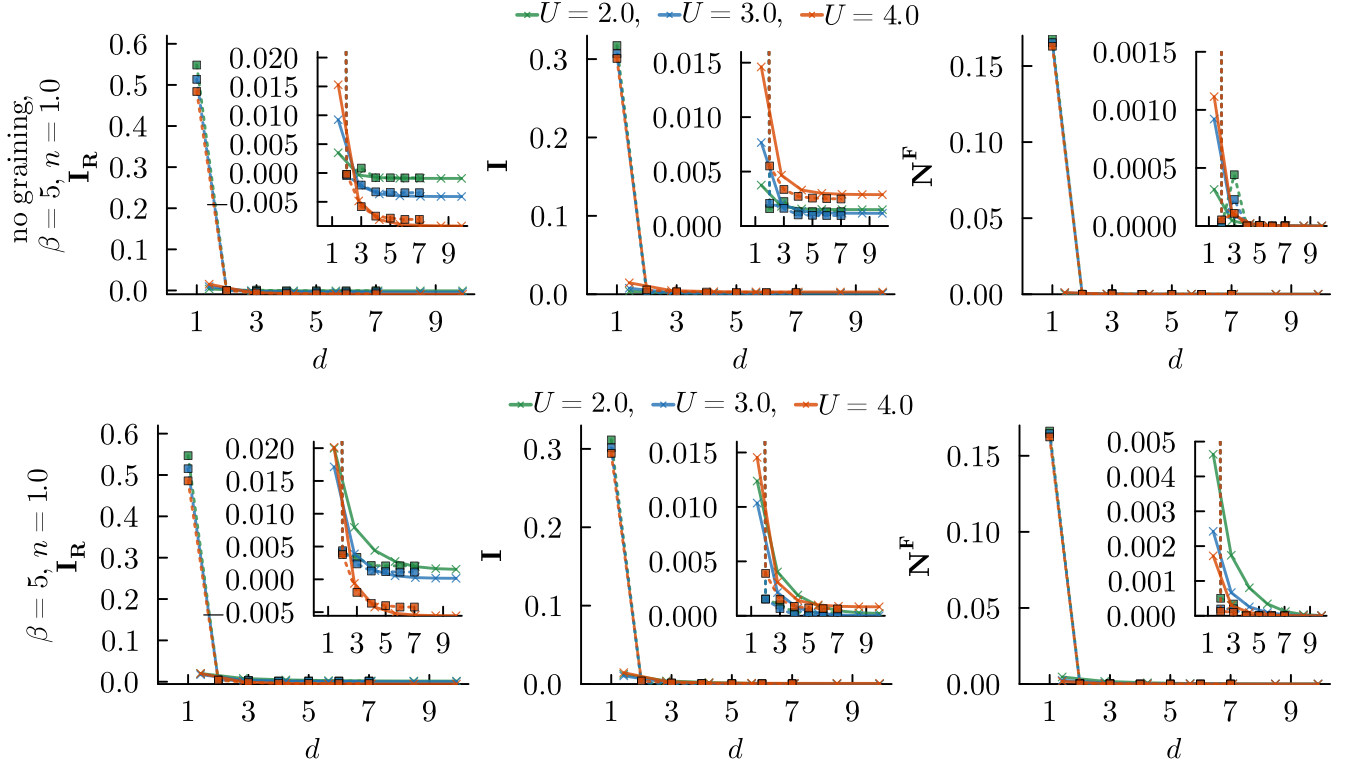


FIG. 8. Same as Fig. 6 but for $U = 2, 3, 4$ at $\beta = 5, n = 1$, comparing no coarse graining (top) to coarse graining (bottom).

in the right panel of Fig. 11.

- ¹ J. S. Bell, *Phys. Phys. Fizika* **1**, 195 (1964).
- ² C. J. Halboth and W. Metzner, *Phys. Rev. Lett.* **85**, 5162 (2000).
- ³ C. Honerkamp, M. Salmhofer, N. Furukawa, and T. M. Rice, *Phys. Rev. B* **63**, 035109 (2001).
- ⁴ E. Gull and A. Millis, *Nature Phys.* **11**, 808 (2015).
- ⁵ M. Kitatani, L. Si, O. Janson, R. Arita, Z. Zhong, and K. Held, *npj Quantum Materials* **5**, 59 (2020).
- ⁶ S. Sakai, Y. Motome, and M. Imada, *Phys. Rev. Lett.* **102**, 056404 (2009).
- ⁷ G. Sordi, P. Sémon, K. Haule, and A.-M. S. Tremblay, *Phys. Rev. Lett.* **108**, 216401 (2012).
- ⁸ F. Šimkovic, R. Rossi, A. Georges, and M. Ferrero, *Science* **385**, eade9194 (2024).
- ⁹ K. Held, R. Peters, and A. Toschi, *Phys. Rev. Lett.* **110**, 246402 (2013).
- ¹⁰ K. Byczuk, M. Kollar, K. Held, Y.-F. Yang, I. A. Nekrasov, T. Pruschke, and D. Vollhardt, *Nature Physics*, 168 (2007).
- ¹¹ J. Kršnik and K. Held, *Nat. Commun.* **16**, 255 (2025).
- ¹² F. Gebhard, *The Mott Metal-insulator transition* (Springer-Verlag (Berlin), 1997).
- ¹³ A. Georges and G. Kotliar, *Phys. Rev. B* **45**, 6479 (1992).
- ¹⁴ P. Hyllus, W. Laskowski, R. Kršček, C. Schwemmer, W. Wicczorek, H. Weinfurter, L. Pezzé, and A. Smerzi, *Phys. Rev. A* **85**, 022321 (2012).
- ¹⁵ P. Hauke, M. Heyl, L. Tagliacozzo, and P. Zoller, *Nat. Phys.* **12**, 778 (2016).
- ¹⁶ F. Mazza, S. Biswas, X. Yan, A. Prokofiev, P. Steffens, Q. Si, F. F. Assaad, and S. Paschen, (2024), [arXiv:2403.12779](#).
- ¹⁷ P. Laurell, A. Scheie, E. Dagotto, and D. A. Tennant, *Adv. Quantum Technol.*, 2400196 (2024).
- ¹⁸ I. Frérot and T. Roscilde, *Phys. Rev. B* **94**, 075121 (2016).
- ¹⁹ F. Bippus, J. Kršnik, M. Kitatani, L. Akšamović, A. Kauch, N. Barišić, and K. Held, (2025), [arXiv:2503.12463](#).
- ²⁰ D. Bałut, X. Guo, N. de Vries, D. Chaudhuri, B. Bradlyn, P. Abbamonte, and P. W. Phillips, (2025), [arXiv:2412.14413](#).
- ²¹ G. Bellomia, *PhD Thesis, SISSA* (2024).
- ²² S. Bera, A. Haldar, and S. Banerjee, *Phys. Rev. B* **109**, 035156 (2024).
- ²³ G. Bellomia, C. Mejuto-Zaera, M. Capone, and A. Amaricci, *Phys. Rev. B* **109**, 115104 (2024).
- ²⁴ C. Walsh, P. Sémon, D. Poulin, G. Sordi, and A.-M. S. Tremblay, *Phys. Rev. Lett.* **122**, 067203 (2019).
- ²⁵ C. Walsh, P. Sémon, D. Poulin, G. Sordi, and A.-M. S. Tremblay, *PRX Quantum* **1**, 020310 (2020).
- ²⁶ G. Roósz, A. Kauch, F. Bippus, D. Wieser, and K. Held, *Phys. Rev. B* **110**, 075115 (2024).
- ²⁷ S. Rohshap and et al., unpublished (2025).

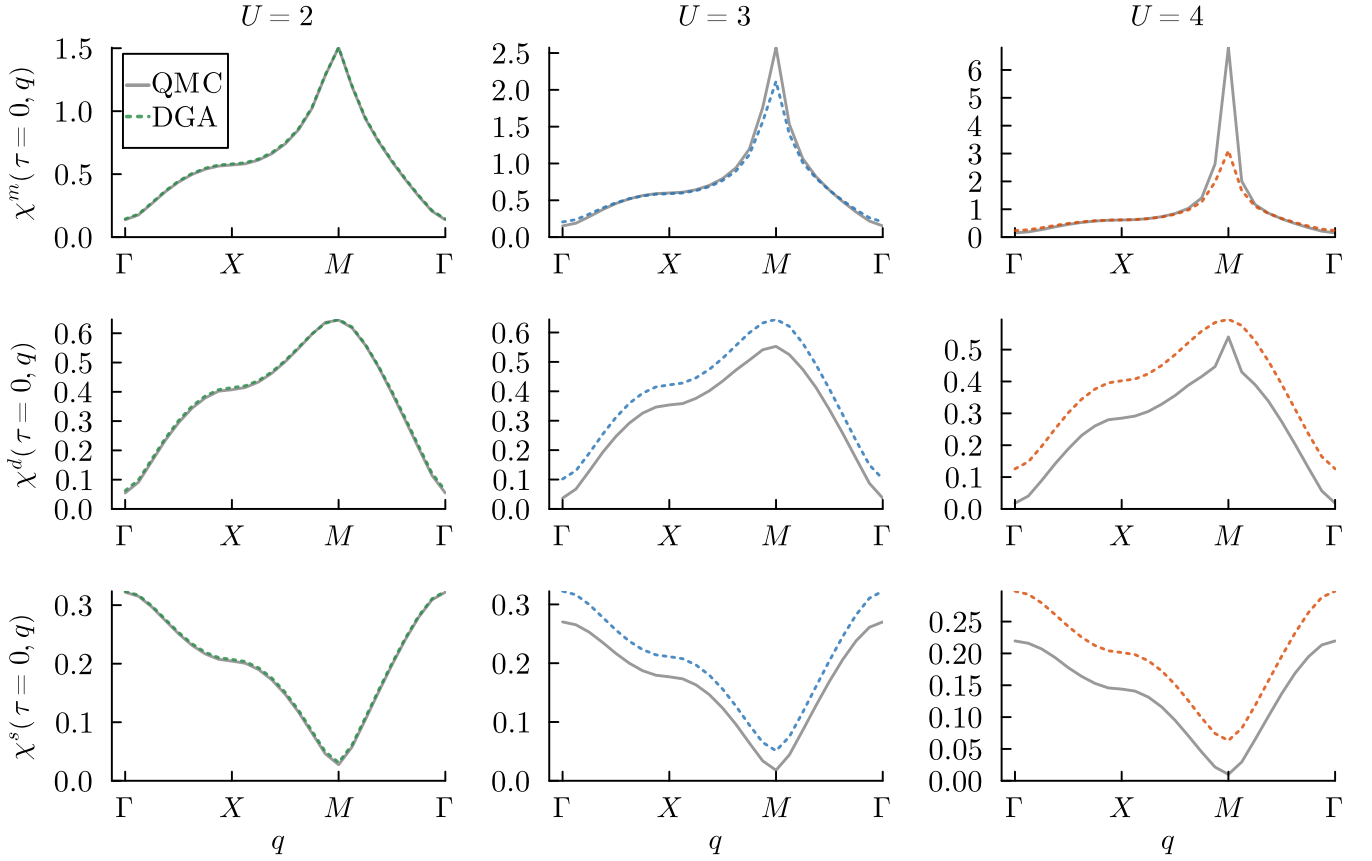


FIG. 9. Comparison of susceptibilities $\chi(\tau = 0, q)$ along high symmetry path $\Gamma - X - M - \Gamma$ obtained with p DGA without coarse-graining (dotted line in color) to QMC (solid grey line). For a) $U = 2$, b) $U = 3$, c) $U = 4$ at $\beta = 5$, $n = 1$.

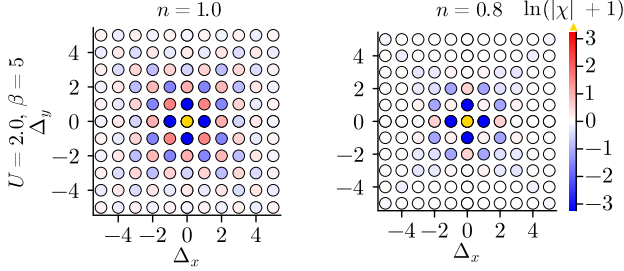


FIG. 10. Susceptibilities at $U = 2$, $\beta = 5$ for $n = 1.0$ and $n = 0.8$. To best visualize the entire data range, we plot $\text{sgn}[\chi^m(\tau = 0, \mathbf{r})] \ln[|\chi^m(\tau = 0, \mathbf{r})| + 1]$.

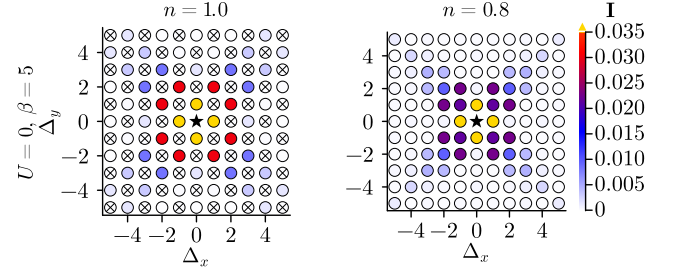


FIG. 11. Left panel: Mutual information in a 1024×1024 non-interacting lattice ($U = 0$), at half-filling and $\beta = 5$. The crosses denote sites where the mutual information is exactly zero, the colorful circles denote the magnitude of the mutual information at the sites where it is non-zero, according to the scale to the right of the figure. Right panel: same as left but at $n = 0.8$.

- ²⁸ C. Gauvin-Ndiaye, J. Tindall, J. R. Moreno, and A. Georges, *Phys. Rev. Lett.* **134**, 076502 (2025).
²⁹ G. Ehlers, J. Sólyom, Ö. Legeza, and R. M. Noack, *Phys. Rev. B* **92**, 235116 (2015).
³⁰ S.-J. Gu, S.-S. Deng, Y.-Q. Li, and H.-Q. Lin, *Phys. Rev. Lett.* **93**, 086402 (2004).
³¹ S. Abaach, Z. Mzaouali, and M. El Baz, *Sci. Rep.* **13** (2023).
³² M. Lo Schiavo, F. Cipriani, G. De Riso, A. Romano, and C. Noce, *J. Magn. Magn. Mater.* **584**, 171066 (2023).
³³ F.-H. Wang and X. Y. Xu, *Nat. Commun.* **16**, 2637 (2025).

- ³⁴ M. Consiglio, J. Odavić, R. Bonsignori, G. Torre, M. Wieśniak, F. Franchini, S. M. Giampaolo, and T. J. G. Apollaro, *Phys. Rev. A* **111**, 032434 (2025).
³⁵ J. D'Emidio, R. Orús, N. Laflorencie, and F. de Juan, *Phys. Rev. Lett.* **132**, 076502 (2024).
³⁶ O. Vafek, N. Regnault, and B. A. Bernevig, *SciPost Phys.* **3** (2017).

- ³⁷ G. De Chiara and A. Sanpera, *Reports on Progress in Physics* **81**, 074002 (2018).
- ³⁸ A. Toschi, A. A. Katanin, and K. Held, *Phys. Rev. B* **75**, 045118 (2007).
- ³⁹ A. Valli, T. Schäfer, P. Thunström, G. Rohringer, S. Andergassen, G. Sangiovanni, K. Held, and A. Toschi, *Phys. Rev. B* **91**, 115115 (2015).
- ⁴⁰ G. Rohringer, H. Hafermann, A. Toschi, A. A. Katanin, A. E. Antipov, M. I. Katsnelson, A. I. Lichtenstein, A. N. Rubtsov, and K. Held, *Rev. Mod. Phys.* **90**, 025003 (2018).
- ⁴¹ W. H. Zurek, *Information Transfer in Quantum Measurements: Irreversibility and Amplification* (Springer US, Boston, MA, 1983).
- ⁴² S. M. Barnett and S. J. D. Phoenix, *Phys. Rev. A* **40**, 2404 (1989).
- ⁴³ A. Peres, *Phys. Rev. Lett.* **77**, 1413 (1996).
- ⁴⁴ M. Horodecki, P. Horodecki, and R. Horodecki, *Phys. Lett. A* **223**, 1 (1996).
- ⁴⁵ H. Shapourian and S. Ryu, *Phys. Rev. A* **99**, 022310 (2019).
- ⁴⁶ H. Shapourian, K. Shiozaki, and S. Ryu, *Phys. Rev. B* **95**, 165101 (2017).
- ⁴⁷ R. Blankenbecler, D. J. Scalapino, and R. L. Sugar, *Phys. Rev. D* **24**, 2278 (1981).
- ⁴⁸ S. White, D. Scalapino, R. Sugar, E. Loh, J. Gubernatis, and R. Scalettar, *Phys. Rev. B* **40**, 506 (1989).
- ⁴⁹ F. Assaad and H. Evertz, in *Computational Many-Particle Physics*, Lecture Notes in Physics, Vol. 739, edited by H. Fehske, R. Schneider, and A. Weiße (Springer, Berlin Heidelberg, 2008) pp. 277–356.
- ⁵⁰ F. F. Assaad, M. Bercx, F. Goth, A. Götz, J. Hofmann, E. Huffman, Z. Liu, F. Parisen Toldin, J. Portela, and J. Schwab, *SciPost Phys. Codebases*, 001 (2022).
- ⁵¹ T. Grover, *Phys. Rev. Lett.* **111**, 130402 (2013).
- ⁵² F. F. Assaad, T. C. Lang, and F. Parisen Toldin, *Phys. Rev. B* **89**, 125121 (2014).
- ⁵³ A. Rényi, *On Measures of Entropy and Information* (University of California Press, 1961).
- ⁵⁴ The Rényi mutual information is based on the generalized Rényi entropy $S_\alpha = \ln(\text{tr} \rho^\alpha)/(1 - \alpha)$. Our definition of the Rényi mutual information eq. (2) corresponds to $\alpha = 2$. For $\alpha = 1$ the original von Neumann entropy and its mutual information eq. (1) is recovered.
- ⁵⁵ M. Kormos and Z. Zimborás, *J. Phys. A: Math. Theor.* **50**, 264005 (2017).
- ⁵⁶ J. Kudler-Flam, *Phys. Rev. Lett.* **130**, 021603 (2023).
- ⁵⁷ G. Vidal and R. F. Werner, *Phys. Rev. A* **65**, 032314 (2002).
- ⁵⁸ M. B. Plenio, *Phys. Rev. Lett.* **95**, 090503 (2005).
- ⁵⁹ J. Eisert, V. Eisler, and Z. Zimborás, *Phys. Rev. B* **97**, 165123 (2018).
- ⁶⁰ A. D. Gottlieb and N. J. Mauser, *Int. J. Quantum Inf.* **05**, 815 (2007).
- ⁶¹ K. Held and N. J. Mauser, *EPJ B* **86**, 328 (2013).
- ⁶² F. Krien, A. Kauch, and K. Held, *Phys. Rev. Res.* **3**, 013149 (2021).
- ⁶³ S. Isakov, H. Terletska, and E. Gull, *Phys. Rev. B* **106**, 235106 (2022).
- ⁶⁴ M. Wallerberger, A. Hausoel, P. Gunacker, A. Kowalski, N. Parragh, F. Goth, K. Held, and G. Sangiovanni, *Comp. Phys. Comm.* **235**, 388 (2019).
- ⁶⁵ C. De Dominicis and P. C. Martin, *Journal of Mathematical Physics* **5**, 14 (1964).
- ⁶⁶ C. De Dominicis and P. C. Martin, *Journal of Mathematical Physics* **5**, 31 (1964).
- ⁶⁷ N. E. Bickers, “Self-consistent many-body theory for condensed matter systems,” in *Theoretical Methods for Strongly Correlated Electrons*, edited by D. Sénéchal, A.-M. Tremblay, and C. Bourbonnais (Springer New York, New York, NY, 2004) pp. 237–296.
- ⁶⁸ F. Krien and A. Kauch, *EPJ B* **95**, 69 (2022).
- ⁶⁹ S. Rohshap, M. K. Ritter, H. Shinaoka, J. von Delft, M. Wallerberger, and A. Kauch, *Phys. Rev. Res.* **7**, 023087 (2025).
- ⁷⁰ F. Krien, A. Valli, and M. Capone, *Phys. Rev. B* **100**, 155149 (2019).
- ⁷¹ Note that only the symmetry-reduced wedge (Δ_x, Δ_y) , $\Delta_x > 0$, $\Delta_x \geq \Delta_y$ has been directly computed in p DfA and the remaining space has been filled by symmetry relations.
- ⁷² C. Hille, F. B. Kugler, C. J. Eckhardt, Y.-Y. He, A. Kauch, C. Honerkamp, A. Toschi, and S. Andergassen, *Phys. Rev. Res.* **2**, 033372 (2020).
- ⁷³ T. Schäfer, N. Wentzell, F. Šimkovic, Y.-Y. He, C. Hille, M. Klett, C. J. Eckhardt, B. Arzhang, V. Harkov, F. m. c.-M. Le Régent, A. Kirsch, Y. Wang, A. J. Kim, E. Kozik, E. A. Stepanov, A. Kauch, S. Andergassen, P. Hansmann, D. Rohe, Y. M. Vilk, J. P. F. LeBlanc, S. Zhang, A.-M. S. Tremblay, M. Ferrero, O. Parcollet, and A. Georges, *Phys. Rev. X* **11**, 011058 (2021).
- ⁷⁴ D. Wieser, *Single-boson exchange decomposition for the extended Hubbard model with application to the optical conductivity*, Master Thesis, TU Wien (2025).
- ⁷⁵ H. Q. Lin and J. E. Hirsch, *Phys. Rev. B* **35**, 3359 (1987).
- ⁷⁶ J. A. Smolin, J. M. Gambetta, and G. Smith, *Phys. Rev. Lett.* **108**, 070502 (2012).
- ⁷⁷ J.-M. Lihm, D. Kiese, S.-S. B. Lee, and F. B. Kugler, (2025), [arXiv:2505.20116](https://arxiv.org/abs/2505.20116).
- ⁷⁸ S. M. Girvin and K. Yang, *Modern Condensed Matter Physics* (Cambridge University Press, 2019).
- ⁷⁹ Y. Ben-Aryeh and A. Mann, *Int. J. Quantum Inf.* **13**, 1550061 (2015).
- ⁸⁰ I. Peschel and V. Eisler, *J. Phys. A: Math. Theor.* **42**, 504003 (2009).